Structural mechanism of Necrocide 1 activation of human TRPM4 that triggers necrosis by sodium overload

Celso M. Teixeira-Duarte[1,2,#], Wan Fu[3,#], Weizhong Zeng[1,2], Jianghuang Wang[3], Xinzhe Jiang[3], Ziye Zhao[3], Qing Zhong[3,*] & Youxing Jiang[1,2,*]

Affiliations:

[1] Howard Hughes Medical Institute and Department of Physiology, University of Texas Southwestern Medical Center, Dallas, Texas, USA

[2] Department of Biophysics, University of Texas Southwestern Medical Center, Dallas, Texas, USA

[3] Institute for Translational Medicine on Cell Fate and Disease, Shanghai Ninth People's Hospital, Key Laboratory of Cell Differentiation and Apoptosis of National Ministry of Education, Department of Pathophysiology, Shanghai Jiao Tong University School of Medicine, Shanghai, China

[#] These authors contribute equally.

[*]Correspondence to:

Youxing Jiang, Ph.D., Department of Physiology, UT Southwestern Medical Center, 5323 Harry Hines Blvd., Dallas, Texas 75390-9040, Tel. 214 645-6027; Fax. 214 645-6042; E-Mail: youxing.jiang@utsouthwestern.edu

Qing Zhong, Ph.D., Department of Pathophysiology, Shanghai Jiao Tong University School of Medicine; Tel. 021-63846590-776429; E-Mail: qingzhong@shsmu.edu.cn

Abstract

The small molecule Necrocide 1 (NC1) constitutively activates human TRPM4, triggering Na^+ influx and leading to necrotic cell death, a process termed *Necrosis by Sodium Overload* (NECSO). NC1 activation is specific to human TRPM4 and does not affect most of the other mammalian TRPM4 orthologs. Here, we elucidate the molecular mechanism underlying NC1 activation and its species-specific selectivity for human TRPM4 using a combination of single-particle cryo-EM, electrophysiology, and cell death assays. We demonstrate that NC1 functions as a non-competitive surrogate of the endogenous Ca^{2+} ligand – it binds to a pocket within the S1-S4 domain adjacent to the Ca^{2+} site and induces the same conformational changes as those triggered by Ca^{2+}. Like Ca^2-mediated activation, NC1-induced channel opening also requires membrane $PI(4,5)P_2$ to stabilize the open state. Through comparative mutagenesis and structural analysis of human and mouse TRPM4, we identify the molecular determinants of NC1 specificity. Our results reveal that the insensitivity of mouse TRPM4 to NC1 arises not from a lack of binding, but from drug-induced conformational changes that destabilize the selectivity filter and inactivate the channel. We identify three critical residues that confer NC1 sensitivity, and their substitution renders mouse TRPM4 responsive to NC1, akin to the human channel. Given the upregulation of TRPM4 in various human cancers, our mechanistic insights into NC1 activation and specificity provide a framework for the potential development of cancer therapeutics targeting TRPM4-mediated necrosis.

Introduction

TRPM4 is a Ca^{2+}-activated, monovalent-selective cation channel belonging to the transient receptor potential melastatin (TRPM) subfamily [1-3]. It is ubiquitously expressed [4] and plays a key role in regulating various physiological processes, including cardiac conduction [5-8], immune response [9], and cell death [10-14]. Notably, TRPM4 is upregulated in several cancer types [15], such as prostate [16-18], breast [19,20], diffuse large B-cell lymphoma [21], and acute myeloid leukemia [22], making it an attractive target for therapeutic intervention. Despite this potential, commonly used TRPM4 modulators suffer from low specificity [5,23-26], prompting extensive efforts to develop monoclonal antibodies [27-30] and small molecules [31,32] specific for this channel. Among the latter, anthranilic acid derivatives, CBA, NBA, and IBA, have emerged as promising inhibitors [31,33,34]. Recent structural studies revealed that NBA and IBA bind in the vanilloid binding pocket, adjacent to the $PI(4,5)P_2$ binding site, to exert their inhibitory effects [34,35].

TRPM4 is activated by intracellular calcium and $PI(4,5)P_2$, promoting membrane depolarization via monovalent cation influx [1,23]. Interestingly, TRPM4 channel opening has been implicated in necrotic cell death triggered by anticancer treatments in human breast cancer cells [12]. Necrocide 1 (NC1) ((S')-3-cycloheptyl-3-(4-hydroxyphenyl)-6-methoxy-7-methyl-1,3-dihydroindole-2-one) is a small molecule derived from the optimization of a compound identified in a screen for anti-tumorigenic activity [36,37]. NC1 induces necrotic cell death in several cancer cell lines, including PC-3 (prostate) and MCF-7 (breast), and has been shown to suppress tumor growth in human cancer xenografts [38]. Importantly, NC1 does not trigger necrosis in non-tumorigenic cells such as fibroblasts and umbilical vein endothelial cells [38].

Recent findings demonstrate that NC1 induces necrotic cell death by directly activating human TRPM4, triggering Na^+ influx that leads to osmotic swelling and membrane rupture, a process termed Necrosis by Sodium Overload (NECSO) [39]. Interestingly, NC1 exhibits a high degree of species specificity: it activates human TRPM4 but not most other mammalian TRPM4 orthologues or other human TRPM family members. Since evading apoptosis is a hallmark of cancer cells [40,41], targeting alternative, non-apoptotic pathways such as TRPM4-mediated necrosis may offer novel therapeutic avenues. Understanding the molecular mechanism of NC1-induced human TRPM4 activation and its species specificity is therefore critical for the rational development of TRPM4-targeted anticancer therapies.

In this study, we combine single-particle cryo-EM, electrophysiology, and cell death assays to elucidate the structural mechanism by which NC1 activates human TRPM4. We identify the NC1 binding site and key molecular determinants responsible for channel activation. In addition, we explain the insensitivity of mouse TRPM4 to NC1 and pinpoint specific residues that define NC1 specificity for human TRPM4, offering insights into the species selectivity of NC1 and paving the way for future therapeutic development.

Results

NC1 activates hTRPM4 and promotes cell death

The small molecule Necrocide 1 (NC1) was recently shown to induce necrotic cell death by activating the human TRPM4 (hTRPM4) channel [39]. The key electrophysiological features of NC1-activated hTRPM4 were characterized using whole-cell patch-clamp recordings of hTRPM4-expressing HEK293 cells (Methods). NC1 activates TRPM4 slowly, requiring about two minutes for the current to reach its maximum, indicating a slow on-rate of NC1 binding (Fig. 1a and 1b). Most channels remain activated even after several minutes of washout, suggesting high-affinity binding and an extremely slow off-rate. With the presence of 1 mM EGTA in the pipette solution (cytosolic side), our recording conditions eliminate the potential contribution to channel activation from cytosolic Ca^{2+}, the endogenous ligand of TRPM4, confirming the Ca^{2+}-independence of NC1 activation.

To complement electrophysiological data, we conducted cell death and viability assays to assess hTRPM4-dependent necrosis in HeLa cells (Methods). While HeLa cells are insensitive to NC1 due to a lack of detectable endogenous TRPM4, they become susceptible to NC1-induced necrosis upon transient or stable expression of hTRPM4. In the cell death assay, EGFP-tagged hTRPM4 was transiently expressed in HeLa cells, and necrotic morphology, characterized by 'balloon-like' cell swelling, was observed 24 hours after NC1 treatment (Fig. 1c). No necrosis was observed in the NC1-treated control cells transiently expressing EGFP or EGFP-tagged mouse TRPM4. This assay provides a qualitative readout of hTRPM4-dependent necrosis, enabling the screening of mutational effects on the NC1 sensitivity of the channel, as discussed later. In the cell viability assay, hTRPM4 was stably expressed in HeLa cells. Following 24-hour NC1 treatment

106 at varying concentrations, cytotoxicity was assessed by measuring intracellular ATP levels,
107 indicative of cell viability, using the CellTiter-Glo (CTG) assay (Fig. 1d, Methods). This assay
108 provides a quantitative measure of NC1's dose-dependent toxicity in hTRPM4-expressing cells.

109

110 **Structure of NC1-bound TRPM4**

111 To elucidate the structural basis of NC1 binding and its activation mechanism, we purified
112 detergent-solubilized hTRPM4 and determined its structure in complex with NC1 at 2.7 Å
113 resolution using single-particle cryo-EM (Fig. 2a, Fig. S1a, Table S1, and Methods). The NC1
114 ligand is unambiguously resolved in the EM density map (Fig. 2b). Occupying a pocket within the
115 S1–S4 domain just above the Ca^{2+} activation site, NC1 forms extensive hydrophobic and
116 hydrogen-bonding interactions with surrounding residues (Fig. 2b).

117 To validate NC1 binding, we performed mutagenesis of residues interacting with the ligand.
118 Due to the extensive contact surface between NC1 and its binding pocket, single-alanine
119 substitutions were insufficient to disrupt NC1 binding and channel activation (Fig. S2a). We
120 therefore introduced bulkier tryptophan substitutions to block NC1 access sterically. Among all
121 tested, three hTRPM4 single-tryptophan mutants - Y790W, L824W, and I909W – completely lost
122 sensitivity to NC1 (Fig. 2c and 2d). These mutants remained responsive to Ca^{2+}/PI(4,5)P_2
123 activation, particularly I909W (Fig. S2b), confirming that these mutations prevent NC1 binding
124 while retaining native activation. The loss of NC1 activation in these mutants was further
125 supported by cell viability assays using stable HeLa cell lines expressing either wild-type or mutant
126 hTRPM4. While NC1 treatment induced a dose-dependent loss of viability in WT-expressing cells,
127 the mutant-expressing cells were resistant to NC1-induced necrosis (Fig. 2e).

128 Despite robust NC1 activation observed in functional assays, the NC1-bound TRPM4
129 structure adopts a conformation intermediate between the closed and open states, when compared
130 to previously determined apo (closed) and Ca^{2+}/PI(4,5)P_2-bound (open) structures (Fig. 3a and Fig.
131 S3a). NC1 binding induces local conformational changes in the S1-S4 domain resembling those
132 triggered by Ca^{2+} (Fig. 3b and Fig. S3b); however, the channel pore and the cytosolic domains
133 remain in a closed conformation (Fig. 3a, 3c, 3d, and Fig. S3a). Within S1-S4, NC1 binding causes
134 the S3 helix to shift inward toward the NC1-binding pocket, moving the W864 side chain closer

135 to the C-terminal end of S4 (Fig. 3b). Through tight packing with H908 on S4, W864 motion
136 displaces the C-terminal part of S4 toward S5 in the adjacent pore domain (Fig. 3b). In the apo
137 TRPM4 structure, F910 at the C-terminal part of S4 forms a key contact with F935 near the
138 cytosolic end of S5 - a coupling essential for transducing Ca^{2+}-induced movements into pore
139 opening, as shown in the Ca^{2+}/PI(4,5)P_2-bound structure [35] (Fig. 3e). In contrast, the NC1-bound
140 structure shows disordered side chains for both F910 and F935, indicating a loss of this critical
141 contact (Fig. 3e). These structural features of NC1-bound hTRPM4, including an activated S1-S4
142 domain, a closed pore, and disrupted F910–F935 coupling, mirror the Ca^{2+}-bound hTRPM4
143 structure in the absence of PI(4,5)P_2, previously proposed to represent a desensitized state [35] (Fig
144 3e and Fig. S3c). Since PI(4,5)P_2 binding is required to stabilize the open state upon Ca^{2+} activation
145 [35], the resemblance between NC1- and Ca^{2+}-bound structures suggests that NC1 triggers local
146 conformational changes similar to those induced by Ca^{2+} and also relies on PI(4,5)P_2 binding to
147 stabilize the open channel.

148

149 **PI(4,5)P_2-dependent NC1 activation of hTRPM4**

150 To test whether PI(4,5)P_2 is indeed required for NC1 activation, we performed patch-clamp
151 recordings of hTRPM4-expressing HEK293 cells in the inside-out configuration. Following initial
152 activation by cytosolic Ca^{2+}, TRPM4 undergoes desensitization to a steady-state level with reduced
153 open probability due to depletion of membrane PI(4,5)P_2, caused by Ca^{2+}-induced phospholipase
154 C activation [42,43] (Fig. 4a). This loss of PI(4,5)P_2 after Ca^{2+} activation creates a condition suitable
155 for assessing NC1 activation in the absence of PI(4,5)P_2. Indeed, hTRPM4 becomes unresponsive
156 to NC1 following PI(4,5)P_2 depletion (Fig. 4a). While PI(4,5)P_2 alone cannot activate TRPM4, its
157 addition in the presence of NC1 robustly activates the channel, restoring current to the pre-
158 desensitization level (Fig. 4a). Consistent with whole-cell recordings, NC1 activates TRPM4
159 slowly in the presence of PI(4,5)P_2, and the ligand remains tightly bound, making it difficult to
160 wash out (Fig. 4b). These results indicate that PI(4,5)P_2 is a prerequisite for NC1-induced
161 activation of hTRPM4.

162 To further support this conclusion, we mutated key positively charged PI(4,5)P_2-interacting
163 residues, R664A, K925A, and K928A, previously identified in the Ca^{2+}/PI(4,5)P_2-activated
164 TRPM4 structure [35]. These mutations significantly impaired NC1 activation in whole-cell

165 recordings, with much stronger effects on inward currents at negative potentials (Fig. 4c and 4d).
166 Additionally, HeLa cells overexpressing these mutants were no longer sensitive to NC1-induced
167 cell death, further validating the requirement of PI(4,5)P_2 for NC1-mediated TRPM4 activation
168 (Fig. 4e and Fig. S4).

169 The PI(4,5)P_2 dependence of NC1-induced hTRPM4 activation was further confirmed by
170 determining the structure of the channel bound to both PI(4,5)P_2 and NC1 at 2.8 Å resolution (Fig.
171 5a and 5b, Fig. S1b, Table S1, and Methods). In this structure, hTRPM4 adopts an open
172 conformation virtually identical to that of the Ca^{2+}/PI(4,5)P_2-activated channel (Fig. 5a). Compared
173 to the structure with NC1 alone, the presence of PI(4,5)P_2 enables the NC1-induced conformational
174 changes within the S1-S4 domain to be effectively transmitted to the pore through the reformation
175 of the critical F910/F935 contact, thereby leading to pore opening (Fig. 3c and 3d and Fig. 5c and
176 5d). This pore-opening movement is further coupled to large-scale rotational and upward swinging
177 motions of the cytosolic domains via the TRP domain, as also observed in the Ca^{2+}/PI(4,5)P_2-
178 activated structure [35] (Fig. 5c and 5e). Interestingly, despite no exogenous Ca^{2+} being added, the
179 canonical Ca^{2+}-binding site within the S1-S4 domain is occupied by a Ca^{2+} ion in the
180 NC1/PI(4,5)P_2-bound structure (Fig. 5b). The stabilized, active conformation of S1-S4 induced by
181 NC1 and PI(4,5)P_2 likely increases the apparent Ca^{2+} affinity, allowing residual micromolar Ca^{2+}
182 in nominally Ca^{2+}-free conditions to bind. To confirm that Ca^{2+} is not required for channel opening
183 in the NC1/PI(4,5)P_2-bound structure, we also determined the structure of the complex prepared
184 in the presence of EGTA (Fig. S1c, Table S1, and Methods). In this case, no bound Ca^{2+} is observed,
185 yet the channel remains in the same open conformation, confirming that NC1 and PI(4,5)P_2 are
186 sufficient to activate the channel independently of Ca^{2+} (Fig. S5a and S5b).

187 Together, these structural and functional results reveal several key insights into PI(4,5)P_2-
188 dependent NC1 activation: NC1 induces conformational changes in the S1-S4 domain similar to
189 those triggered by Ca^{2+} without interfering with Ca^{2+} binding; Like Ca^{2+}, NC1 alone stabilizes the
190 channel in a desensitized state, requiring PI(4,5)P_2 to promote channel opening; In the presence of
191 PI(4,5)P_2, both NC1 and Ca^{2+} can independently activate hTRPM4.

192

193

194 **Molecular determinants of NC1 specificity for human TRPM4**

195 NC1 activates human but not mouse TRPM4 [39], despite the high sequence and structural
196 homology between the two orthologs. This species-specific activation is particularly intriguing
197 given the identical amino acid composition and conserved structure of the NC1-binding pocket.
198 To identify the molecular determinants underlying this specificity, we used the cell death assay to
199 screen various mutations in both human and mouse TRPM4 expressed in HeLa cells. Through a
200 combination of chimeric constructs and point mutations (Fig. S6, Fig. S7, and associated legends),
201 we identified three residues that potentially contribute to the selective activation of hTRPM4 by
202 NC1: V904 on the S4 helix (corresponding to L900 in mTRPM4), P997 in the pore domain (R993
203 in mTRPM4), and R1064 on the TRP helix (S1060 in mTRPM4) (Fig. 6a).

204 We next tested whether mouse TRPM4 could be converted into an NC1-sensitive channel
205 by introducing single, double, and triple mutations in which the three residues (L900, R993, and
206 S1060) were replaced with their human TRPM4 counterparts. Figure 6b and 6c show the
207 electrophysiological recordings of NC1 activation in these mutants. Strikingly, the single S1060R
208 mutation in mTRPM4 was sufficient to confer NC1 sensitivity; however, the resulting current was
209 outwardly rectifying, with greater conductance at depolarized membrane potentials. In contrast,
210 mTRPM4 mutants bearing L900V and/or R993P substitutions remained insensitive to NC1 when
211 tested individually or in combination. Notably, when these mutations were combined with S1060R,
212 NC1 sensitivity was significantly enhanced. The mTRPM4 triple mutant (L900V/R993P/S1060R)
213 displayed an NC1 activation profile nearly identical to that of hTRPM4. Complementing these
214 gain-of-function experiments, we also tested loss-of-function mutations in hTRPM4 (Fig. S8a and
215 S8b). Consistent with the mTRPM4 mutagenesis findings, mutations at V904 and P997 did not
216 affect NC1 activation of hTRPM4. In contrast, both the single R1064S mutation and the
217 V904L/P997R/R1064S triple mutation significantly reduced NC1 activation, though not
218 completely abolishing it.

219 In addition, we generated the HeLa stable cell lines expressing those mTRPM4 gain-of-
220 function mutants and measured their viability in response to NC1 treatment (Fig. 6d). Consistent
221 with our electrophysiology result, expressing mTRPM4 with L900V and R993P mutations has
222 little effect on cell viability similar to control cells expressing WT mTRPM4 or empty vector;
223 however, the expression of S1060R single mutant or S1060R-containing double or triple mutants

224 progressively decreases the cell viability in response to NC1; cells expressing the
225 L900V/R993P/S1060R triple mutant of mTRPM4 exhibit similar sensitivity to NC1-induced
226 necrosis as hTRPM4-expressing cells.

227

228 **The structural basis of NC1 specificity**

229 To gain structural insight into the NC1 specificity of TRPM4, we determined the cryo-EM
230 structures of both the NC1-insensitive WT mTRPM4 and its NC1-activated
231 L900V/R993P/S1060R triple mutant, each in the presence of NC1 (Fig. S9, Table S2, and
232 Methods). As PI(4,5)P_2 is required for NC1 activation in hTRPM4, it was also included during
233 mTRPM4 protein preparation (Methods).

234 The structure of WT mTRPM4 in the presence of NC1 and PI(4,5)P_2 was resolved at 2.9
235 Å resolution (Fig. 7a). Surprisingly, NC1 still binds to mTRPM4 at the same pocket as in hTRPM4
236 with identical surrounding residues (Fig. 7b), despite failing to activate the channel. Relative to
237 the apo mTRPM4 structure, NC1 binding induces similar local conformational changes within the
238 S1-S4 domain, as observed in hTRPM4 (Fig. S10a). However, unlike NC1/PI(4,5)P_2-activated
239 hTRPM4, where large swinging and rotational movements of the cytosolic domains are coupled
240 to pore opening, the cytosolic domains of NC1/PI(4,5)P_2-bound mTRPM4 closely resemble the
241 apo closed conformation, with only a subtle rigid-body shift (Fig. 7a). Notably, three distinct
242 conformational changes in the transmembrane region of NC1/PI(4,5)P_2-bound mTRPM4
243 distinguish it from the NC1-sensitive hTRPM4 and likely underlie its lack of activation (Fig. 7c,
244 7d and 7e). Firstly, the entire S1-S4 domain moves laterally toward the center of the channel (Fig.
245 7c). Secondly, the central filter and surrounding pore helices exhibit no clear density, suggesting
246 the filter becomes disordered upon NC1 binding (Fig. 7d) - a surprising finding, as this tightly
247 packed central filter region remains steady during channel gating and is typically the best-resolved
248 in TRPM4 structures. Thirdly, the S5 helix shifts inward toward the filter, while the pore-lining
249 S6 helix moves outward, widening the intracellular gate (Fig. 7c and 7e).

250 The latter two structural changes appear to originate from the lateral movement of S1-S4.
251 Due to tight S5-mediated packing between the S1-S4 domain and the neighboring subunit's pore
252 domain, this lateral shift of S1-S4 drives S5 inward, compressing the adjacent pore helix and filter

253 toward the central axis (Fig. 7c). Unable to accommodate this compression, the filter likely
254 undergoes a promiscuous movement and adopts a disordered, non-conductive conformation,
255 leading to the collapse of the ion conduction pathway. The accompanying outward motion of S6
256 likely serves to relieve the spatial strain caused by the rearrangement of the central pore.
257 Importantly, these conformational changes are solely induced by NC1 binding, as an NC1-bound
258 mTRPM4 structure prepared without PI(4,5)P_2 is identical to the NC1/PI(4,5)P_2-bound form (Fig.
259 S9b, Fig. S10b, Table S2, and Methods). Thus, the insensitivity of mTRPM4 to NC1 activation is
260 not due to a lack of drug binding, but rather to NC1-induced collapse of the selectivity filter,
261 rendering the channel non-conductive, analogous to C-type inactivation observed in certain K^+
262 channels [44].

263 We next determined the structure of the NC1-sensitive mTRPM4 triple mutant
264 (L900V/R993P/S1060R) in complex with NC1 and PI(4,5)P_2 (Fig. 7f, Fig. S9c, Table S2, and
265 Methods). Unlike WT mTRPM4, the mutant's pore domain is well structured and adopts an open
266 conformation (Fig. 7e), and its S1-S4 domain no longer undergoes a lateral movement. The overall
267 structure of the mutant closely resembles that of the NC1/PI(4,5)P_2-bound open hTRPM4 (Fig.
268 S10c), faithfully recapitulating the activation mechanism observed in the human channel. Given
269 that the S1060R mutation in the TRP helix is the key determinant for conferring NC1 sensitivity,
270 we focused our structural comparison on this region between NC1/PI(4,5)P_2-bound WT and
271 mutant mTRPM4. In the mutant, R1060 forms a network of inter-domain interactions absent in
272 the WT channel (Fig. 7g). Specifically, R1060 mediates a cluster of salt bridges and hydrogen
273 bonds involving D858 and W860 at the N-terminus of S3, as well as the glycerol phosphate head
274 group of PI(4,5)P_2. These interactions serve to stabilize the S1-S4 domain, preventing the inward
275 lateral movement observed in NC1-bound WT mTRPM4 that disrupts the pore. Notably, this
276 arginine residue, crucial for NC1 sensitivity, is conserved in human and primate TRPM4 orthologs
277 but is replaced by a serine in most other mammalian species.

278

279 **Discussion**

280 The small molecule NC1 activates hTRPM4, triggering Na^+ influx and leading to necrotic
281 cell death via sodium overload. Through structural and functional analyses, we elucidated the
282 molecular mechanism underlying NC1-mediated activation of hTRPM4. NC1 binds near the Ca^{2+}

activation site within the S1-S4 domain and induces local conformational changes that mirror those caused by Ca^{2+}. Like Ca^{2+}, NC1 requires membrane PI(4,5)P_2 to stabilize the open channel conformation. Thus, NC1 acts as a non-competitive surrogate of the native ligand. NC1 engages in extensive hydrophobic and polar interactions with surrounding residues, resulting in high-affinity binding. Its binding site, deeply buried within the protein, likely contributes to its slow activation kinetics and poor washout. While distinct from the binding sites of other known TRPM4 modulators, the NC1 site is similar to some modulator-binding pockets in TRPM3 (e.g., primidone and CIM 0216) [45,46] and TRPM8 (e.g., N-(3-aminopropyl)-2-[(3-methylphenyl)methoxy]-N-[(thiophen-2-yl)methyl]benzamide (AMTB), cryosim-3 (C3), icilin, and the menthol analog WS-12) [47-49].

NC1 selectively activates human TRPM4 but not most other mammalian TRPM4 orthologs. Through comparative studies of human and mouse TRPM4, we determined that the species specificity of NC1 activation is not due to a failure in drug binding. Instead, in mTRPM4, NC1 binding destabilizes the selectivity filter, rendering the channel non-conductive, akin to C-type inactivation observed in certain K^+ channels. We identified R1064, located on the TRP helix of hTRPM4, as a key determinant of NC1 specificity. This arginine mediates a network of interdomain interactions that stabilize the S1-S4 domain's lateral position within the membrane. In TRPM4s from mice and most other mammals, a serine occupies this position. The absence of arginine-mediated stabilization permits a lateral shift of the S1-S4 domain upon NC1 binding, which collapses the selectivity filter and inactivates the channel. Interestingly, akin to NC1, the TRPM4 modulator CBA was shown to inhibit the human but not the mouse channel [33] and does not exert any effect on other TRPM channel subfamily members [31]. However, the mechanistic details that confer TRPM4 species-specificity to this compound have not been thoroughly explored.

The mechanistic insights into NC1 activation of hTRPM4 and its remarkable specificity revealed in this study establish a structural framework for understanding how small molecules can selectively modulate TRPM4 function. Our structural analyses identify a previously unrecognized drug-binding pocket that is distinct from those of other known TRPM4 modulators, thereby expanding the current understanding of ligand recognition and channel activation in the TRPM family. The defined NC1-binding mode provides an essential molecular basis for rational drug

312 design aimed at exploiting TRPM4-mediated necrosis as a potential therapeutic avenue for cancer
313 treatment.

314 The discovery that NC1 binds to an identical site in both human and mouse TRPM4
315 orthologs but induces markedly different functional outcomes emphasizes the structural subtleties
316 governing allosteric coupling and species-dependent channel gating. Given the widespread
317 reliance on murine and other mammalian models in preclinical studies, our findings underscore
318 the necessity of validating compound efficacy and mechanism in human-derived systems to ensure
319 accurate interpretation of pharmacological responses. This cross-species discrepancy also serves
320 as a cautionary example for drug development pipelines targeting ion channels, where even small
321 structural variations can result in divergent functional consequences. Collectively, our results
322 provide a comprehensive molecular foundation for future high-throughput screening, structure-
323 guided optimization, and in vivo evaluation of TRPM4 modulators.

Methods

Protein expression and purification

Full-length wild-type human TRPM4 (UniProtKB: Q8TD43) containing an N-terminal FLAG-tag (DYKDDDDK) and full-length wild-type or L900V;R993P;S1060R mouse TRPM4 (UniprotKB: Q7TN37) containing a C-terminal FLAG-tag were cloned into a pEZT-BM plasmid [50]. *E.coli* DH10Bac cells were used to synthesize the bacmid that was employed in baculovirus production in Sf9 cells (Thermo Fisher Scientific) using Cellfectin II reagent (Thermo Fisher Scientific). For protein expression, HEK293S GnTI$^-$ cells (American Type Culture Collection (ATCC), CRL-3022) grown in suspension to a density of $3x10^6$ cells/mL were infected with P3 viruses at a ratio of 1:40 (virus:cell, v/v) and supplemented with 10 mM sodium butyrate to boost protein expression. The cells were then incubated at 37 °C for 48 h before being harvested by centrifugation (5000 g, 15 min, 4 °C). The cell pellet was resuspended in lysis buffer (50 mM Tris-HCl pH 7.5, 150 mM NaCl) supplemented with protease inhibitors (0.5 µg/ml pepstatin, 2 µg/ml leupeptin, 1 µg/ml aprotinin, and 1 mM PMSF) and homogenized by sonication. TRPM4 was then extracted with 1 % (w/v) lauryl maltose neopentyl glycol (LMNG, Anatrace) in gentle agitation for 2 h at 4 °C. The supernatant was subsequently collected by centrifugation (40000 g, 40 min, 4 °C) and incubated with Anti-DYKDDDDK G1 Affinity Resin (GenScript) for 1 h and 30 min at 4 °C in gentle agitation. The resin was then washed with Buffer A (50 mM Tris-HCl pH 7.5, 150 mM NaCl, 0.01 % LMNG) and elution was performed by incubating for 45 min at room temperature in gentle agitation with Buffer B (50 mM Tris-HCl pH 7.5, 150 mM NaCl, 0.01 % LMNG, 0.2 mg/mL FLAG peptide). The eluate was then concentrated and further purified by size-exclusion chromatography in Buffer C (50 mM Tris-HCl pH 7.5, 150 mM NaCl, 0.0035 % LMNG) on a Superose 6 Increase 10/300 GL (GE Healthcare). For the Ca^{2+} free samples, 2 mM EGTA was also included in Buffer C and for the samples requiring $PI(4,5)P_2$, 50 µM Brain $PI(4,5)P_2$ (L-α-phosphatidylinositol-4,5-bisphosphate (Brain, Porcine) (ammonium salt), Avanti) was added to the buffer B during the elution step and further used to supplement the concentrated eluate before size-exclusion chromatography.

Cryo-EM sample preparation and data acquisition

352 hTRPM4 and mTRPM4 samples were concentrated to ~7-8 mg/mL and supplemented with 0.3
353 mM Necrocide 1 ((S')-3-cycloheptyl-3-(4-hydroxyphenyl)-6-methoxy-7-methyl-1,3-
354 dihydroindole-2-one) (NC1). 1 mM EGTA was also added when required. Supplemented samples
355 were incubated for 1 h on ice before vitrification. 4 µL was then applied to a glow-discharged
356 Quantifoil R1.2/1.3 300-mesh gold holey carbon grid (Quantifoil, Micro Tools GmbH, Germany),
357 blotted for 3.5 s under 100 % humidity at 12 °C and plunged into liquid ethane using a Mark IV
358 Vitrobot (FEI).

359 All data collections were performed using SerialEM with a nominal defocus range set from -0.9
360 to -2.2 µm and each movie was recorded with a total dose of 60 $e^-/Å^2$.

361 For the dataset of hTRPM4 containing NC1 and EGTA, movies were acquired on a Titan Krios
362 microscope (FEI) operated at 300 kV with a Falcon4i direct electron detector camera (Thermo
363 Fisher Scientific) at 0.738 Å pixel size.

364 For the dataset of hTRPM4 containing NC1 and PI(4,5)P_2, movies were acquired on a Titan Krios
365 microscope (FEI) operated at 300 kV with a K3 direct electron detector camera (Gatan) using the
366 CDS (Correlated Double Sampling) mode with a super-resolution pixel size of 0.4172 Å.

367 For the datasets of hTRPM4 containing NC1, PI(4,5)P_2 and EGTA and mTRPM4 wild-type
368 containing NC1 and PI(4,5)P_2, movies were acquired on a Titan Krios microscope (FEI) operated
369 at 300 kV with a K3 direct electron detector camera (Gatan) using the CDS (Correlated Double
370 Sampling) mode with a super-resolution pixel size of 0.4285 Å.

371 For the datasets of mTRPM4 wild-type containing NC1 and mTRPM4 L900V/R993P/S1060R
372 triple mutant containing NC1 and PI(4,5)P_2, movies were acquired on a Titan Krios microscope
373 (FEI) operated at 300 kV with a Falcon4i direct electron detector camera (Thermo Fisher Scientific)
374 at 0.735 Å pixel size.

375 **Cryo-EM data processing**

376 The workflow for data processing is summarized in Fig. S1 and Fig. S9. Data processing was
377 performed using cryoSPARC (versions 4.3.1 or 4.4.1) [51] following the general scheme described
378 below with some modifications between the datasets. For the dataset of hTRPM4 containing NC1
379 and PI(4,5)P_2, RELION (version 3.1) [52,53] was also employed in the processing workflow.

380 For the dataset of hTRPM4 containing NC1 and PI(4,5)P_2, movies were motion-corrected and
381 dose-weighted using MotionCor2 [54] and CTF estimation was performed using GCTF [55].
382 Micrographs were manually inspected to remove those with bad defocus values and ice
383 contamination. Particles were then picked using Laplacian-of-Gaussian (LoG) and extracted in
384 RELION. Extracted particles were subjected to multiple rounds of 2D classification and classes
385 displaying clear features of the TRPM4 channel were used for subsequent 3D classification. The
386 particles from the best-resolving 3D classes along with the respective 3D volumes were then
387 imported into cryoSPARC and used for 3D heterogeneous refinement and 3D classification
388 without alignment to remove junk particles and differentiate channel conformations. The best-
389 resolving 3D classes were refined using Non-Uniform refinement with imposed C4 symmetry [56].

390 For all other datasets, movies were subjected to patch motion correction and subsequent patch CTF
391 estimation in cryoSPARC. The resulting micrographs were manually curated and those exhibiting
392 drift, poor CTF estimation and outliers in defocus values and ice thickness were excluded from
393 further processing (individually assessed for each parameter relative to the overall distribution).
394 An initial round of particle picking was carried out with blob picker. Particles were then extracted
395 and subjected to one round of 2D classification. Classes displaying clear features of the TRPM4
396 channel were selected and used either directly for subsequent processing or to re-pick particles
397 with template picker. Additional rounds of 2D classification were further performed and particles
398 from selected classes were used to obtain an initial 3D reconstruction with Ab-Initio. 3D
399 heterogeneous refinement was then employed to remove junk particles, and the resulting particles
400 were subjected to 3D classification without alignment to differentiate channel conformations. The
401 best-resolving 3D classes were refined using Non-Uniform refinement with imposed C4 symmetry
402 [56].

403 Map resolutions were reported according to the gold-standard Fourier shell correlation (FSC) using
404 the 0.143 criterion [57]. Local resolutions and angular distributions were estimated in cryoSPARC.

405 **Model building**

406 Initial models were obtained using a combination of ModelAngelo [58] and previously available
407 hTRPM4 (PDBs: 9MTA and 9MRT) and mTRPM4 (PDB:6BCJ) structures. The models were then
408 manually adjusted in Coot [59] and refined against the respective maps in PHENIX [60]. Ligand
409 restraints CIF files were generated using the Grade2 Web Server [61]. The geometry statistics of the

410 models were obtained using MolProbity [62]. All the structural figures were prepared using UCSF
411 ChimeraX [63,64].

412 **Electrophysiology**

413 Wild-type human and mouse TRPM4, along with the respective mutants, were cloned into a
414 pEGFP-N1 plasmid (Clontech). Mutants were generated by site-directed mutagenesis using the
415 QuickChange method and verified by sequencing. 1 μg of plasmid was transfected into HEK293
416 cells using Lipofectamine 2000 (Life Technology). 48 h after transfection, cells were dissociated
417 by trypsin treatment and kept in a complete serum-containing medium before being re-plated onto
418 35-mm tissue culture dishes and incubated in a tissue culture incubator until recording.

419 Channel currents were recorded in whole cell or excised inside-out configuration. The long-chain
420 native Brain PI(4,5)P_2 employed in the structural studies is insoluble in water and forms liposomes
421 in the recording solutions, making it difficult to fuse into the patch membrane. Therefore, the
422 water-soluble short-chain synthetic PI(4,5)P_2 diC8 (Phosphatidylinositol 4,5-bisphosphate diC8,
423 Echelon Bioscience) was used in the functional experiments as needed. For inside-out patches, the
424 standard bath solution (cytosolic side) contained (in mM): 145 caesium methanesulfonate (Cs–
425 MS), 5 NaCl, 1 $MgCl_2$, 0.3 $CaCl_2$, 10 HEPES buffered with Tris, pH 7.4. 10 μM NC1 and/or 10
426 μM PI(4,5)P_2 diC8 were added to the bath solution when required. For the calcium-free condition,
427 0.5 mM EGTA was added to the bath solution without $CaCl_2$. The pipette solution (extracellular
428 side) contained (in mM): 140 Na–MS, 1 $MgCl_2$, 5 $CaCl_2$, 10 HEPES buffered with Tris, pH 7.4.
429 For whole cell current recordings, the pipette solution contained (in mM): Cs-MS 140, CsCl 4,
430 $MgCl_2$ 1, EGTA 1 or 10, HEPES 10, buffered with Tris, pH 7.4. Bath solution contained (in mM):
431 Na-MS 140, NaCl 5, $MgCl_2$ 1, $CaCl_2$ 1, HEPES 10, buffered with Tris, pH=7.4. 10 μM NC1 was
432 added to the bath solution as needed. Patch pipettes were pulled from borosilicate glass (Harvard
433 Apparatus) and heat polished to a resistance of 3–5 MΩ. After the patch pipette was attached to
434 the cell membrane, a giga seal (> 10 GΩ) was formed by gentle suction. The inside-out
435 configuration was formed by pulling the pipette away from the cell and the pipette tip was exposed
436 to air for a short time in some cases. The holding potential was set to 0 mV. The current and voltage
437 relationship (I–V curve) was obtained using voltage pulses ramped from – 100 to + 100 mV over
438 an 800 ms duration every 2 seconds. Data was acquired using an AxoPatch 200B amplifier
439 (Molecular Devices) and a low-pass analog filter set to 1 kHz. The current signal was sampled at

440 a rate of 20 kHz using a Digidata 1322A digitizer (Molecular Devices) and further analyzed with
441 pClamp 11 software (Molecular Devices). Sample traces for the I–V curves of macroscopic
442 currents shown were obtained from recordings on the same patch. Bars represent mean ± SEM of
443 five measurements from different patches (n = 5 independent biological replicates).

444 **Cell death assay**

445 Cell death was assessed in HeLa cells transiently expressing EGFP-tagged human or mouse
446 TRPM4 by monitoring the morphological change of transfected cells using microscopy, as
447 described previously [39]. Briefly, HeLa cells were seeded onto glass coverslips and grown to 30–
448 40% confluency before transfection. 24 hours after TRPM4-EGFP transfection, cells were
449 subjected to 1 μM NC1 treatment. Fluorescence images were taken before and after the indicated
450 period of treatment. The morphological changes of cells with green fluorescence were monitored
451 using microscopy, and over 50 cells expressing TRPM4 were analyzed in each group.

452 **Cell viability assay**

453 Cell viability was assessed in HeLa cells stably expressing human or mouse TRPM4, using the
454 CellTiter-Glo (CTG) assay as described previously [39]. Briefly, cells were seeded in a 96-well plate
455 at a density of $1x10^4$ cells per well and allowed to adhere overnight. After treatment with various
456 experimental conditions, the intracellular ATP was measured using the CTG luminescent assay kit
457 (Promega, G7570) according to the manufacturer's instructions. Briefly, 100 μL of CTG reagent
458 was added to each well, and the plate was gently shaken for 10 minutes to induce cell lysis and
459 release of intracellular ATP. The luminescence signal, proportional to the amount of ATP present
460 and indicative of cell viability, was measured using a multi-well plate reader. All experiments were
461 repeated three times, and the results were presented as mean ± SD.

462

463 ## Data availability

464 The cryo-EM density maps of the human TRPM4 have been deposited in the Electron Microscopy
465 Data Bank (EMDB) under accession numbers EMD-73526 (NC1-bound in the presence of EGTA),
466 EMD-73527 (NC1/PI(4,5)P_2-bound), and EMD-73528 (NC1/PI(4,5)P_2-bound in the presence of
467 EGTA). Atomic coordinates have been deposited in the Protein Data Bank (PDB) under accession

468 numbers 9YVK (NC1-bound in the presence of EGTA), 9YVL (NC1/PI(4,5)P_2-bound), and
469 9YVM (NC1/PI(4,5)P_2-bound in the presence of EGTA).

470 The cryo-EM density maps of the mouse TRPM4 have been deposited in the Electron Microscopy
471 Data Bank (EMDB) under accession numbers EMD-73530 (NC1/PI(4,5)P_2-bound wild-type
472 mTRPM4), EMD-73529 (NC1-bound wild-type mTRPM4), and EMD-73531 (NC1/PI(4,5)P_2-
473 bound L900V/R993P/S1060R triple mutant mTRPM4). Atomic coordinates have been deposited
474 in the Protein Data Bank (PDB) under accession numbers 9YVO (NC1/PI(4,5)P_2-bound wild-type
475 mTRPM4), 9YVN (NC1-bound wild-type mTRPM4), and 9YVP (NC1/PI(4,5)P_2-bound
476 L900V/R993P/S1060R triple mutant mTRPM4).

477

478 ## Acknowledgements

479 Single particle cryo-EM data were collected at the University of Texas Southwestern Medical
480 Center Cryo-EM Facility (CEMF) funded by the CPRIT Core Facility Support Award RP170644
481 and at Howard Hughes Medical Institute Janelia Cryo-EM Facility. Cryo-EM sample grids were
482 prepared at the Structural Biology Laboratory at UT Southwestern Medical Center partially
483 supported by grant RP170644 from CPRIT. This work was supported in part by the Howard
484 Hughes Medical Institute (to Y.J.) and by grant from the National Institute of Health
485 (R35GM140892 to Y.J.), and by grants from MOST (Ministry of Science and Technology of the
486 People's Republic of China) (2023YFA0914900 to Q.Z.), NSFC (National Natural Science
487 Foundation of China) (92254307 to Q.Z.).

488

489 ## Competing interests

490 The authors declare no competing interests.

491

492 # References

493 1 Launay, P. *et al.* TRPM4 is a Ca2+-activated nonselective cation channel mediating cell
494 membrane depolarization. *Cell* **109**, 397-407 (2002). https://doi.org/10.1016/s0092-
495 8674(02)00719-5
496 2 Montell, C. *et al.* A Unified Nomenclature for the Superfamily of TRP Cation Channels. *Molecular*
497 *Cell* **9**, 229-231 (2002). https://doi.org/https://doi.org/10.1016/S1097-2765(02)00448-3
498 3 Nilius, B. *et al.* Voltage dependence of the Ca2+-activated cation channel TRPM4. *J Biol Chem*
499 **278**, 30813-30820 (2003). https://doi.org/10.1074/jbc.M305127200
500 4 Fonfria, E. *et al.* Tissue Distribution Profiles of the Human TRPM Cation Channel Family. *Journal*
501 *of Receptors and Signal Transduction* **26**, 159-178 (2006).
502 https://doi.org/10.1080/10799890600637506
503 5 Demion, M., Bois, P., Launay, P. & Guinamard, R. TRPM4, a Ca2+-activated nonselective cation
504 channel in mouse sino-atrial node cells. *Cardiovasc Res* **73**, 531-538 (2007).
505 https://doi.org/10.1016/j.cardiores.2006.11.023
506 6 Guinamard, R., Demion, M., Chatelier, A. & Bois, P. Calcium-Activated Nonselective Cation
507 Channels in Mammalian Cardiomyocytes. *Trends in Cardiovascular Medicine* **16**, 245-250 (2006).
508 https://doi.org/https://doi.org/10.1016/j.tcm.2006.04.007
509 7 Hof, T. *et al.* TRPM4 non-selective cation channel variants in long QT syndrome. *BMC Med Genet*
510 **18**, 31 (2017). https://doi.org/10.1186/s12881-017-0397-4
511 8 Stallmeyer, B. *et al.* Mutational spectrum in the Ca2+-activated cation channel gene TRPM4 in
512 patients with cardiac conductance disturbances. *Human Mutation* **33**, 109-117 (2012).
513 https://doi.org/https://doi.org/10.1002/humu.21599
514 9 Launay, P. *et al.* TRPM4 regulates calcium oscillations after T cell activation. *Science* **306**, 1374-
515 1377 (2004). https://doi.org/10.1126/science.1098845
516 10 Becerra, A. *et al.* Transient receptor potential melastatin 4 inhibition prevents
517 lipopolysaccharide-induced endothelial cell death. *Cardiovascular Research* **91**, 677-684 (2011).
518 https://doi.org/10.1093/cvr/cvr135
519 11 Gerzanich, V. *et al.* De novo expression of Trpm4 initiates secondary hemorrhage in spinal cord
520 injury. *Nature Medicine* **15**, 185-191 (2009). https://doi.org/10.1038/nm.1899
521 12 Ghosh, S. *et al.* Plasma Membrane Channel TRPM4 Mediates Immunogenic Therapy-Induced
522 Necrosis. *Cancer Res* **83**, 3115-3130 (2023). https://doi.org/10.1158/0008-5472.Can-23-0157
523 13 Schattling, B. *et al.* TRPM4 cation channel mediates axonal and neuronal degeneration in
524 experimental autoimmune encephalomyelitis and multiple sclerosis. *Nature Medicine* **18**, 1805-
525 1811 (2012). https://doi.org/10.1038/nm.3015
526 14 Simon, F. *et al.* Hydrogen peroxide removes TRPM4 current desensitization conferring increased
527 vulnerability to necrotic cell death. *J Biol Chem* **285**, 37150-37158 (2010).
528 https://doi.org/10.1074/jbc.M110.155390
529 15 Borgström, A., Peinelt, C. & Stokłosa, P. TRPM4 in Cancer-A New Potential Drug Target.
530 *Biomolecules* **11** (2021). https://doi.org/10.3390/biom11020229
531 16 Berg, K. D. *et al.* TRPM4 protein expression in prostate cancer: a novel tissue biomarker
532 associated with risk of biochemical recurrence following radical prostatectomy. *Virchows Archiv*
533 **468**, 345-355 (2016). https://doi.org/10.1007/s00428-015-1880-y
534 17 Holzmann, C. *et al.* Transient receptor potential melastatin 4 channel contributes to migration of
535 androgen-insensitive prostate cancer cells. *Oncotarget* **6** (2015).
536 18 Sagredo, A. I. *et al.* TRPM4 channel is involved in regulating epithelial to mesenchymal
537 transition, migration, and invasion of prostate cancer cell lines. *Journal of Cellular Physiology*
538 **234**, 2037-2050 (2019). https://doi.org/https://doi.org/10.1002/jcp.27371

539 19 Guo, J. *et al.* TRPM4 channels contribute to Adriamycin chemoresistance in breast cancer cells.
540 *European Journal of Pharmacology* **998**, 177637 (2025).
541 https://doi.org/https://doi.org/10.1016/j.ejphar.2025.177637
542 20 Wong, K. K. & Hussain, F. A. TRPM4 is overexpressed in breast cancer associated with estrogen
543 response and epithelial-mesenchymal transition gene sets. *PLOS ONE* **15**, e0233884 (2020).
544 https://doi.org/10.1371/journal.pone.0233884
545 21 Loo, S. K. *et al.* TRPM4 expression is associated with activated B cell subtype and poor survival in
546 diffuse large B cell lymphoma. *Histopathology* **71**, 98-111 (2017).
547 https://doi.org/10.1111/his.13204
548 22 Wang, F. *et al.* Aberrant TRPM4 expression in MLL-rearranged acute myeloid leukemia and its
549 blockade induces cell cycle arrest via AKT/GLI1/Cyclin D1 pathway. *Cellular Signalling* **72**, 109643
550 (2020). https://doi.org/https://doi.org/10.1016/j.cellsig.2020.109643
551 23 Amarouch, M.-Y., Syam, N. & Abriel, H. Biochemical, single-channel, whole-cell patch clamp, and
552 pharmacological analyses of endogenous TRPM4 channels in HEK293 cells. *Neuroscience Letters*
553 **541**, 105-110 (2013). https://doi.org/https://doi.org/10.1016/j.neulet.2013.02.011
554 24 Burris, S. K., Wang, Q., Bulley, S., Neeb, Z. P. & Jaggar, J. H. 9-Phenanthrol inhibits recombinant
555 and arterial myocyte TMEM16A channels. *Br J Pharmacol* **172**, 2459-2468 (2015).
556 https://doi.org/10.1111/bph.13077
557 25 Gardam, K. E., Geiger, J. E., Hickey, C. M., Hung, A. Y. & Magoski, N. S. Flufenamic acid affects
558 multiple currents and causes intracellular Ca2+ release in Aplysia bag cell neurons. *J*
559 *Neurophysiol* **100**, 38-49 (2008). https://doi.org/10.1152/jn.90265.2008
560 26 Guinamard, R. *et al.* Functional characterization of a Ca2+-activated non-selective cation channel
561 in human atrial cardiomyocytes. *The Journal of Physiology* **558**, 75-83 (2004).
562 https://doi.org/https://doi.org/10.1113/jphysiol.2004.063974
563 27 Chen, B. *et al.* TRPM4-specific blocking antibody attenuates reperfusion injury in a rat model of
564 stroke. *Pflugers Arch* **471**, 1455-1466 (2019). https://doi.org/10.1007/s00424-019-02326-8
565 28 Low, S. W. *et al.* Development and characterization of a monoclonal antibody blocking human
566 TRPM4 channel. *Sci Rep* **11**, 10411 (2021). https://doi.org/10.1038/s41598-021-89935-5
567 29 Wei, S. *et al.* Binding epitope for recognition of human TRPM4 channel by monoclonal antibody
568 M4M. *Scientific Reports* **12**, 19562 (2022). https://doi.org/10.1038/s41598-022-22077-4
569 30 Wei, S. *et al.* Development and in vitro characterization of humanized antibodies for blocking
570 human TRPM4 channel. *Sci Rep* **15**, 19769 (2025). https://doi.org/10.1038/s41598-025-05256-x
571 31 Ozhathil, L. C. *et al.* Identification of potent and selective small molecule inhibitors of the cation
572 channel TRPM4. *Br J Pharmacol* **175**, 2504-2519 (2018). https://doi.org/10.1111/bph.14220
573 32 Binkle-Ladisch, L. *et al.* Identification and development of TRPM4 antagonists to counteract
574 neuronal excitotoxicity. *iScience* **27**, 111425 (2024). https://doi.org/10.1016/j.isci.2024.111425
575 33 Arullampalam, P. *et al.* Species-Specific Effects of Cation Channel TRPM4 Small-Molecule
576 Inhibitors. *Front Pharmacol* **12**, 712354 (2021). https://doi.org/10.3389/fphar.2021.712354
577 34 Ekundayo, B. *et al.* Identification of a binding site for small molecule inhibitors targeting human
578 TRPM4. *Nat Commun* **16**, 833 (2025). https://doi.org/10.1038/s41467-025-56131-2
579 35 Teixeira-Duarte, C. M., Zeng, W. & Jiang, Y. Structural landscape of activation, desensitization
580 and inhibition in the human TRPM4 channel. *Nature Structural & Molecular Biology* (2025).
581 https://doi.org/10.1038/s41594-025-01705-3
582 36 Christensen, M. K. *et al.* Synthesis and antitumor effect in vitro and in vivo of substituted 1,3-
583 dihydroindole-2-ones. *J Med Chem* **53**, 7140-7145 (2010). https://doi.org/10.1021/jm100763j
584 37 Trojel-Hansen, C. *et al.* Novel small molecule drugs inhibit tumor cell metabolism and show
585 potent anti-tumorigenic potential. *Cancer Chemother Pharmacol* **68**, 127-138 (2011).
586 https://doi.org/10.1007/s00280-010-1453-3

587 38 Zhang, J. *et al.* Necrocide 1 mediates necrotic cell death and immunogenic response in human
588 cancer cells. *Cell Death Dis* **14**, 238 (2023). https://doi.org/10.1038/s41419-023-05740-0
589 39 Fu, W. *et al.* Persistent activation of TRPM4 triggers necrotic cell death characterized by sodium
590 overload. *Nature Chemical Biology* (2025). https://doi.org/10.1038/s41589-025-01841-3
591 40 Fulda, S. & Debatin, K. M. Extrinsic versus intrinsic apoptosis pathways in anticancer
592 chemotherapy. *Oncogene* **25**, 4798-4811 (2006). https://doi.org/10.1038/sj.onc.1209608
593 41 Singh, R., Letai, A. & Sarosiek, K. Regulation of apoptosis in health and disease: the balancing act
594 of BCL-2 family proteins. *Nature Reviews Molecular Cell Biology* **20**, 175-193 (2019).
595 https://doi.org/10.1038/s41580-018-0089-8
596 42 Nilius, B. *et al.* The Ca2+-activated cation channel TRPM4 is regulated by phosphatidylinositol
597 4,5-biphosphate. *Embo j* **25**, 467-478 (2006). https://doi.org/10.1038/sj.emboj.7600963
598 43 Zhang, Z., Okawa, H., Wang, Y. & Liman, E. R. Phosphatidylinositol 4,5-bisphosphate rescues
599 TRPM4 channels from desensitization. *J Biol Chem* **280**, 39185-39192 (2005).
600 https://doi.org/10.1074/jbc.M506965200
601 44 Ong, S. T., Tyagi, A., Chandy, K. G. & Bhushan, S. Mechanisms Underlying C-type Inactivation in
602 Kv Channels: Lessons From Structures of Human Kv1.3 and Fly Shaker-IR Channels. *Frontiers in*
603 *Pharmacology* **Volume 13 - 2022** (2022). https://doi.org/10.3389/fphar.2022.924289
604 45 Yin, Y. *et al.* Molecular basis of neurosteroid and anticonvulsant regulation of TRPM3. *Nature*
605 *Structural & Molecular Biology* **32**, 828-840 (2025). https://doi.org/10.1038/s41594-024-01463-
606 8
607 46 Kumar, S. *et al.* Structural basis for agonist and heat activation of nociceptor TRPM3. *Nature*
608 *Structural & Molecular Biology* (2025). https://doi.org/10.1038/s41594-025-01692-5
609 47 Yin, Y. *et al.* Structural basis of cooling agent and lipid sensing by the cold-activated TRPM8
610 channel. *Science* **363**, eaav9334 (2019). https://doi.org/doi:10.1126/science.aav9334
611 48 Yin, Y. *et al.* Mechanisms of sensory adaptation and inhibition of the cold and menthol receptor
612 TRPM8. *Science Advances* **10**, eadp2211 (2024). https://doi.org/doi:10.1126/sciadv.adp2211
613 49 Zhao, C. *et al.* Structures of a mammalian TRPM8 in closed state. *Nature Communications* **13**,
614 3113 (2022). https://doi.org/10.1038/s41467-022-30919-y
615 50 Morales-Perez, C. L., Noviello, C. M. & Hibbs, R. E. Manipulation of Subunit Stoichiometry in
616 Heteromeric Membrane Proteins. *Structure* **24**, 797-805 (2016).
617 https://doi.org/10.1016/j.str.2016.03.004
618 51 Punjani, A., Rubinstein, J. L., Fleet, D. J. & Brubaker, M. A. cryoSPARC: algorithms for rapid
619 unsupervised cryo-EM structure determination. *Nature Methods* **14**, 290-296 (2017).
620 https://doi.org/10.1038/nmeth.4169
621 52 Scheres, S. H. W. RELION: Implementation of a Bayesian approach to cryo-EM structure
622 determination. *Journal of Structural Biology* **180**, 519-530 (2012).
623 https://doi.org/https://doi.org/10.1016/j.jsb.2012.09.006
624 53 Zivanov, J. *et al.* New tools for automated high-resolution cryo-EM structure determination in
625 RELION-3. *Elife* **7** (2018). https://doi.org/10.7554/eLife.42166
626 54 Zheng, S. Q. *et al.* MotionCor2: anisotropic correction of beam-induced motion for improved
627 cryo-electron microscopy. *Nature Methods* **14**, 331-332 (2017).
628 https://doi.org/10.1038/nmeth.4193
629 55 Zhang, K. Gctf: Real-time CTF determination and correction. *Journal of Structural Biology* **193**, 1-
630 12 (2016). https://doi.org/https://doi.org/10.1016/j.jsb.2015.11.003
631 56 Punjani, A., Zhang, H. & Fleet, D. J. Non-uniform refinement: adaptive regularization improves
632 single-particle cryo-EM reconstruction. *Nature Methods* **17**, 1214-1221 (2020).
633 https://doi.org/10.1038/s41592-020-00990-8

57 Henderson, R. *et al.* Outcome of the first electron microscopy validation task force meeting. *Structure* **20**, 205-214 (2012). https://doi.org/10.1016/j.str.2011.12.014

58 Jamali, K. *et al.* Automated model building and protein identification in cryo-EM maps. *Nature* **628**, 450-457 (2024). https://doi.org/10.1038/s41586-024-07215-4

59 Emsley, P., Lohkamp, B., Scott, W. G. & Cowtan, K. Features and development of Coot. *Acta Crystallographica Section D* **66**, 486-501 (2010). https://doi.org/doi:10.1107/S0907444910007493

60 Liebschner, D. *et al.* Macromolecular structure determination using X-rays, neutrons and electrons: recent developments in Phenix. *Acta Crystallographica Section D* **75**, 861-877 (2019). https://doi.org/doi:10.1107/S2059798319011471

61 Smart, O. S., Sharff A., Holstein, J., Womack, T.O., Flensburg, C., Keller, P., Paciorek, W., Vonrhein, C. and Bricogne G. Grade2 version 1.6.0. *Cambridge, United Kingdom:Global Phasing Ltd.* (2021).

62 Chen, V. B. *et al.* MolProbity: all-atom structure validation for macromolecular crystallography. *Acta Crystallogr D Biol Crystallogr* **66**, 12-21 (2010). https://doi.org/10.1107/s0907444909042073

63 Pettersen, E. F. *et al.* UCSF ChimeraX: Structure visualization for researchers, educators, and developers. *Protein Sci* **30**, 70-82 (2021). https://doi.org/10.1002/pro.3943

64 Meng, E. C. *et al.* UCSF ChimeraX: Tools for structure building and analysis. *Protein Science* **32**, e4792 (2023). https://doi.org/https://doi.org/10.1002/pro.4792

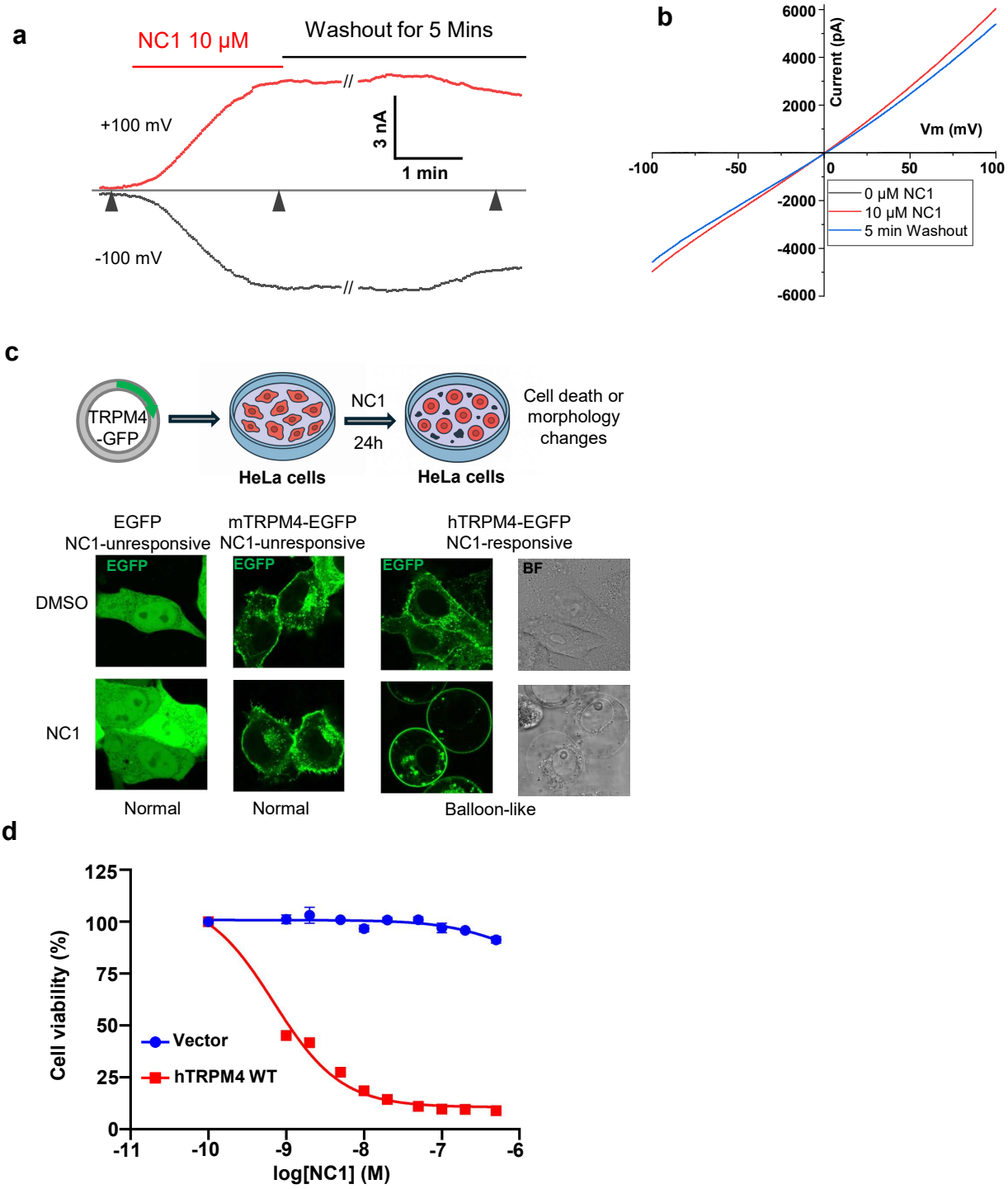

Fig. 1: NC1 activation of hTRPM4. a Macroscopic currents of hTRPM4 overexpressed in HEK293 cells at ±100 mV in a whole-cell patch with the presence or absence of 10 μM NC1 in the bath (extracellular). Triangles mark the time points of three NC1-mediated hTRPM4 activation states (left to right): Closed channel in the absence of NC1; Fully activated channel 2 min after NC1 addition; Channel current retained 5 min after NC1 washout. **b** Sample I-V curves measured at the time points marked by the triangles shown in **a**. **c** NC1-induced cell death assay. Top panel: schematic illustration of the assay. Bottom panels: morphologies of EGFP, EGFP-tagged mTRPM4, or EGFP-tagged hTRPM4-expressing HeLa cells 24 hours after DMSO (NC1 solvent) or NC1 (1 μM) treatment. **d** Dose-dependent NC1 cytotoxicity in HeLa cells stably expressing wild-type hTRPM4. Data points represent mean ± SD of n = 3 independent replicates.

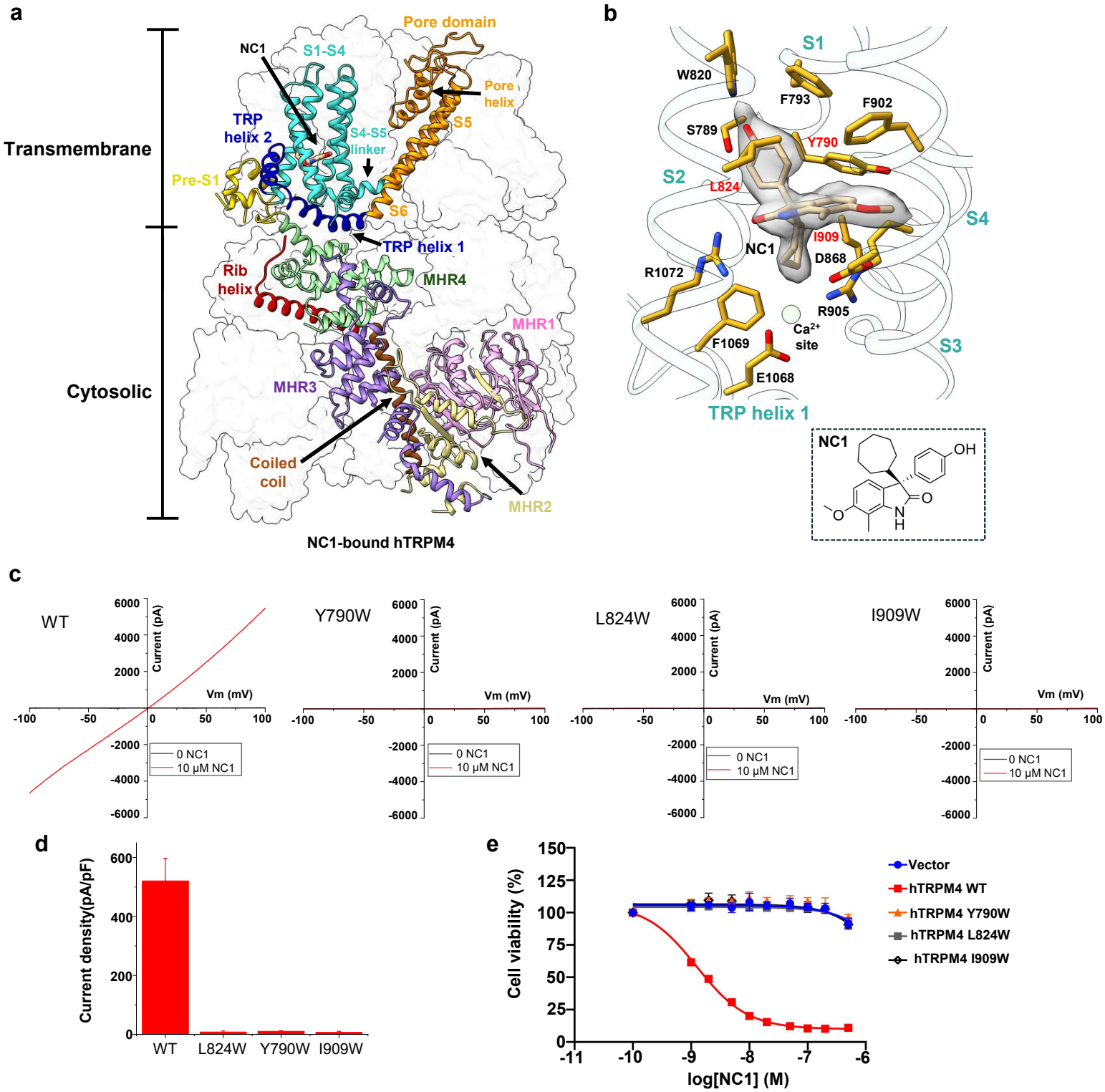

Fig. 2: NC1 binding in hTRPM4. a Structure of NC1-bound hTRPM4. The front subunit is depicted in a cartoon representation, with each domain individually colored. **b** Zoomed-in view of the NC1 binding site. NC1 and its surrounding residues are shown in stick representation. The light green sphere marks the calcium activation site. NC1 density (grey surface) is contoured at 0.2 in ChimeraX. Residues sensitive to tryptophan substitution are labeled in red. **c** Sample I-V curves of wild-type hTRPM4 and its tryptophan substitutions at the NC1-binding site recorded in whole-cell patches with 10 μM NC1 in the bath (extracellular). **d** Outward current density of NC1-activated wild-type hTRPM4 and its tryptophan mutations recorded at +100 mV in whole-cell patches with 10 μM NC1 in the bath (extracellular). Bars represent mean ± SEM of n=5 independent replicates. **e** Dose-dependent NC1 cytotoxicity in HeLa cells stably expressing wild-type hTRPM4 or its tryptophan mutations. Data points represent mean ± SD of n = 3 independent replicates.

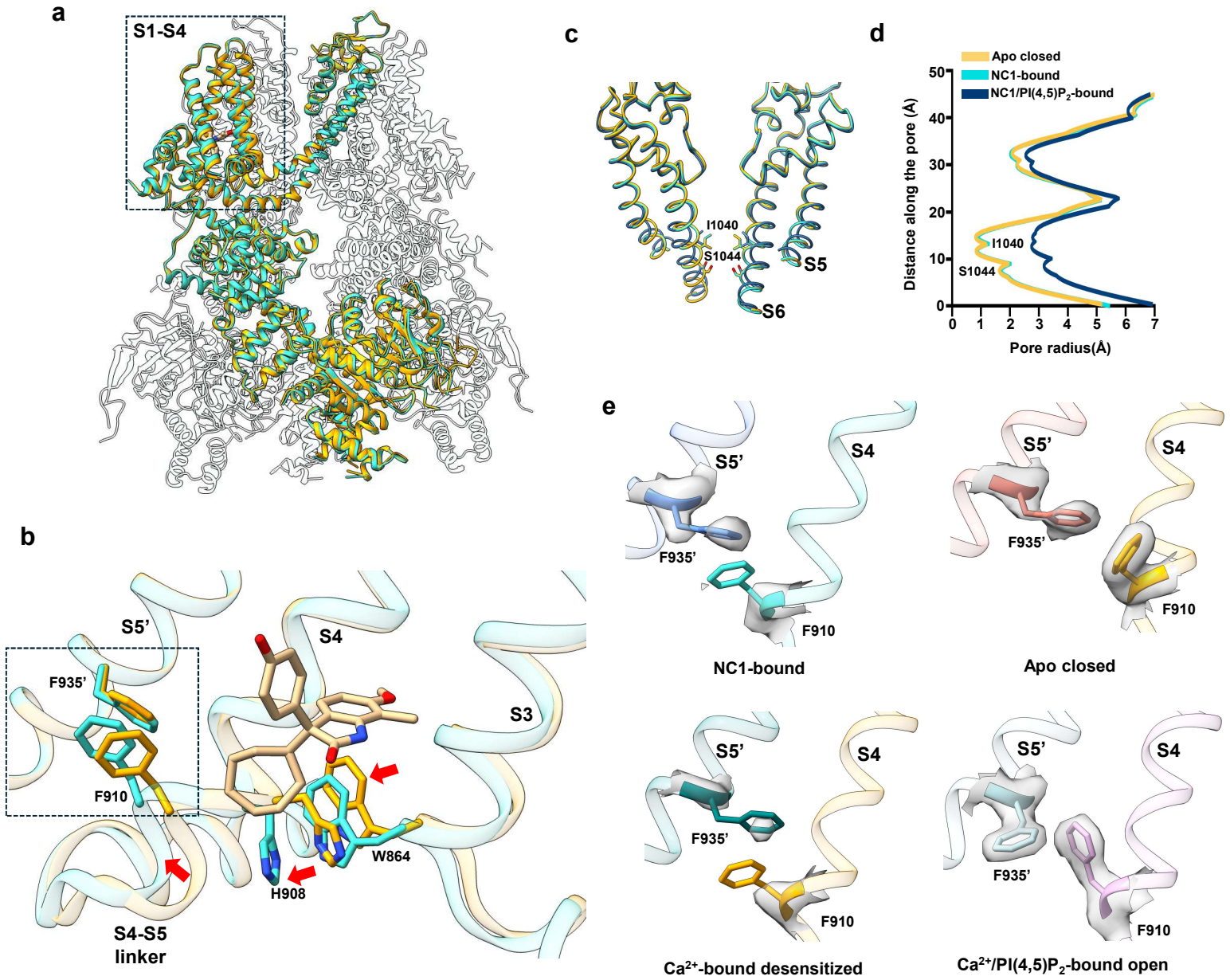

Fig. 3: hTRPM4 conformational changes induced by NC1 binding. a Superposition of the hTRPM4 structures in the NC1-bound and apo closed (PDB:9MTA) states with the front subunits highlighted in cyan and orange, respectively. **b** Local conformational changes at the S1-S4 domain between NC1-bound (cyan) and apo closed (orange) hTRPM4. Only S3-S4 and the neighboring S5 (marked with a single quotation mark) are displayed for clarity. Red arrows mark the major movements upon NC1 binding. Key residues are shown in stick representation. **c** Structural comparison of the hTRPM4 ion conduction pore in the apo closed (orange), NC1-bound (cyan), and NC1/PI(4,5)P_2-bound (navy blue) states. Gating residues I1040 and S1044 are shown in stick representation. The front and back subunits are removed for clarity. **d** Pore radius of hTRPM4 along the central axis in the apo closed, NC1-bound, and NC1/PI(4,5)P_2-bound structures. **e** F935'-F910 contact interface in the NC1-bound, apo closed, Ca^{2+}-bound desensitized (PDB:9MT8), and Ca^{2+}/PI(4,5)P_2-bound open (PDB:9MRT) states. The EM density maps for F910 and F935' are shown in grey surface contoured at 0.23 in ChimeraX.

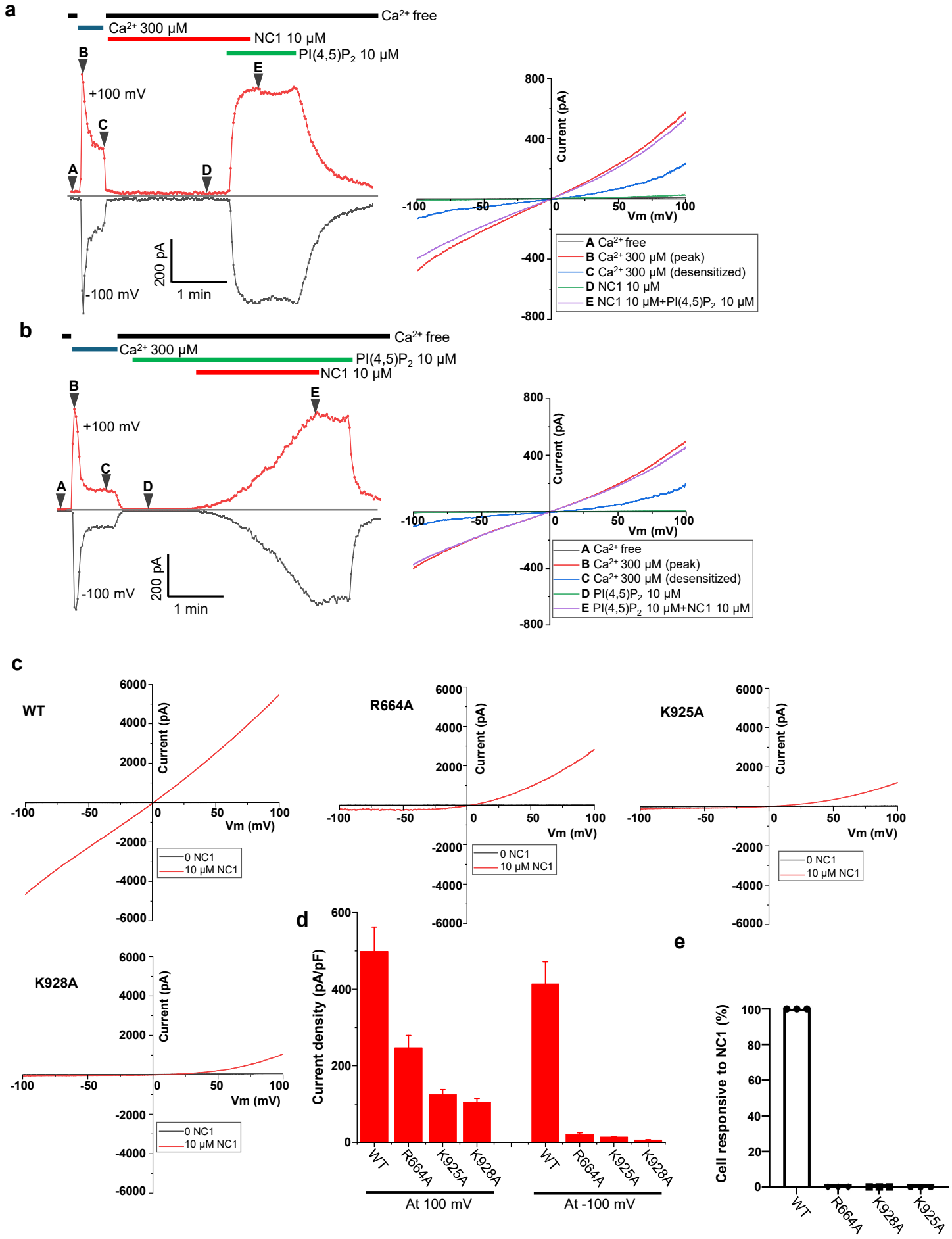
a
Ca2+ free
Ca2+ 300 μM
NC1 10 μM
PI(4,5)P2 10 μM
B
E
+100 mV
C
A
D
-100 mV
200 pA
1 min
Current (pA)
Vm (mV)
A Ca2+ free
B Ca2+ 300 μM (peak)
C Ca2+ 300 μM (desensitized)
D NC1 10 μM
E NC1 10 μM+PI(4,5)P2 10 μM
b
Ca2+ free
Ca2+ 300 μM
PI(4,5)P2 10 μM
NC1 10 μM
B
E
+100 mV
C
A
D
-100 mV
200 pA
1 min
Current (pA)
Vm (mV)
A Ca2+ free
B Ca2+ 300 μM (peak)
C Ca2+ 300 μM (desensitized)
D PI(4,5)P2 10 μM
E PI(4,5)P2 10 μM+NC1 10 μM
c
WT
R664A
K925A
K928A
Current (pA)
Vm (mV)
0 NC1
10 μM NC1
d
Current density (pA/pF)
WT
R664A
K925A
K928A
At 100 mV
At -100 mV
e
Cell responsive to NC1 (%)
WT
R664A
K928A
K925A

Fig. 4 PI(4,5)P_2-dependent NC1 activation of hTRPM4. a Macroscopic currents of hTRPM4-expressing HEK293 cells at ±100 mV in an inside-out patch with the presence or absence of Ca^{2+}, NC1, and PI(4,5)P_2 diC8 in the bath (cytosolic). NC1 and PI(4,5)P_2 diC8 were introduced after Ca^{2+} activation and desensitization due to Ca^{2+}-induced membrane PI(4,5)P_2 depletion. A-E mark the time points of hTRPM4 in various states: A, apo closed state; B, initial Ca^{2+}-activated state before desensitization; C, Ca^{2+}-bound desensitized state due to PI(4,5)P_2 depletion; D, closed state in the presence of NC1; E, NC1/PI(4,5)P_2-activated state. The panel on the right depicts sample I-V curves corresponding to A-E time points. **b** Similar recordings as **a** except that PI(4,5)P_2 diC8 was introduced before NC1, and the time point D marks the closed state in the presence of PI(4,5)P_2 diC8. The panel on the right depicts sample I-V curves corresponding to A-E time points. **c** Sample I-V curves of wild-type hTRPM4 and its alanine substitutions at the PI(4,5)P_2-binding site recorded in whole-cell patches with 10 μM NC1 in the bath (extracellular). **d** Outward and inward current densities of NC1-activated wild-type hTRPM4 and its mutants recorded at ±100 mV in whole-cell patches with 10 μM NC1 in the bath (extracellular). Bars represent mean ± SEM of n=5 independent replicates. **e** Responsiveness of HeLa cells to NC1-induced cell death when expressing wild-type hTRPM4 or its PI(4,5)P_2 site mutants. Data points represent mean ± SD of n = 3 independent replicates. Over 50 cells were counted in each replicate.

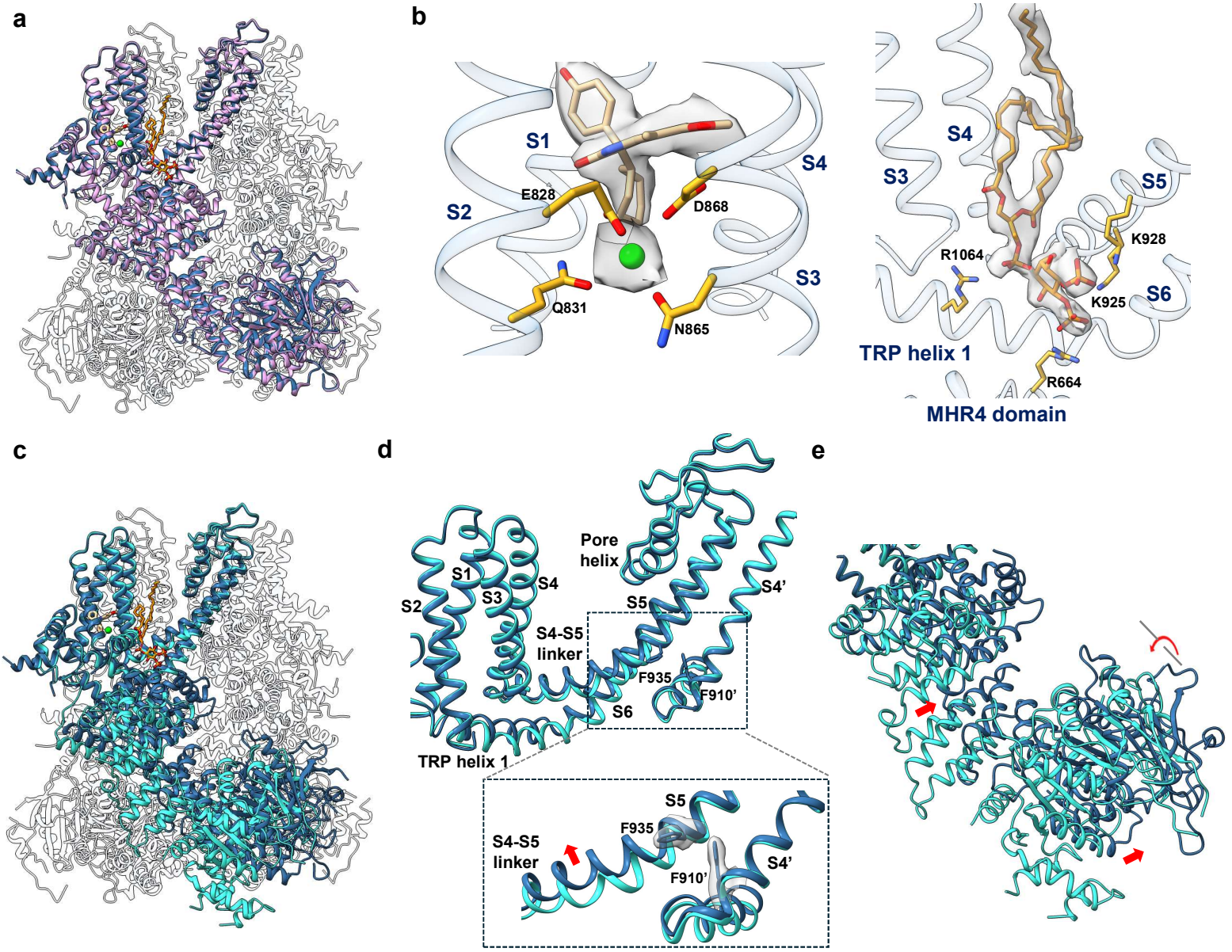

Fig. 5: Structure of NC1/PI(4,5)P_2-bound hTRPM4. a Superposition of the NC1/PI(4,5)P_2-bound and Ca^{2+}/PI(4,5)P_2-bound (PDB:9MRT) hTRPM4 open structures with the front subunits highlighted in navy blue and pink, respectively. NC1 and PI(4,5)P_2 are depicted in stick representation, and Ca^{2+} is shown as a green sphere. **b** Zoomed-in view of the ligand binding sites in the NC1/PI(4,5)P_2-bound structure. Ca^{2+} is represented as a green sphere. NC1, PI(4,5)P_2, and ligand-interacting residues are shown in stick representation. Density (grey surface) is contoured at 0.5 for NC1 and Ca^{2+} and at 0.45 for PI(4,5)P_2 in ChimeraX. **c** Superposition of the NC1/PI(4,5)P_2-bound open and NC1-bound hTRPM4 structures with the front subunits highlighted in navy blue and cyan, respectively. **d** Enlarged view of the conformational changes at the transmembrane region between the NC1/PI(4,5)P_2-bound open (navy blue) and NC1-bound (cyan) structures. The S4 helix from the neighboring subunit (S4') is also shown. The inset shows a close-up highlighting the coupling between F935 and neighboring F910' in the NC1/PI(4,5)P_2-bound structure that leads to the movement (red arrow) at the S4-S5 linker and S5 and channel opening. Density for F935 and F910' is shown in a grey surface and contoured at 0.55 in ChimeraX. **e** Conformational changes at the cytosolic MHR domains between the NC1/PI(4,5)P_2-bound (navy blue) and NC1-bound (cyan) structures. Red arrows mark the upward swing of the cytosolic MHR domains and the rotation of MHRs 1 and 2.

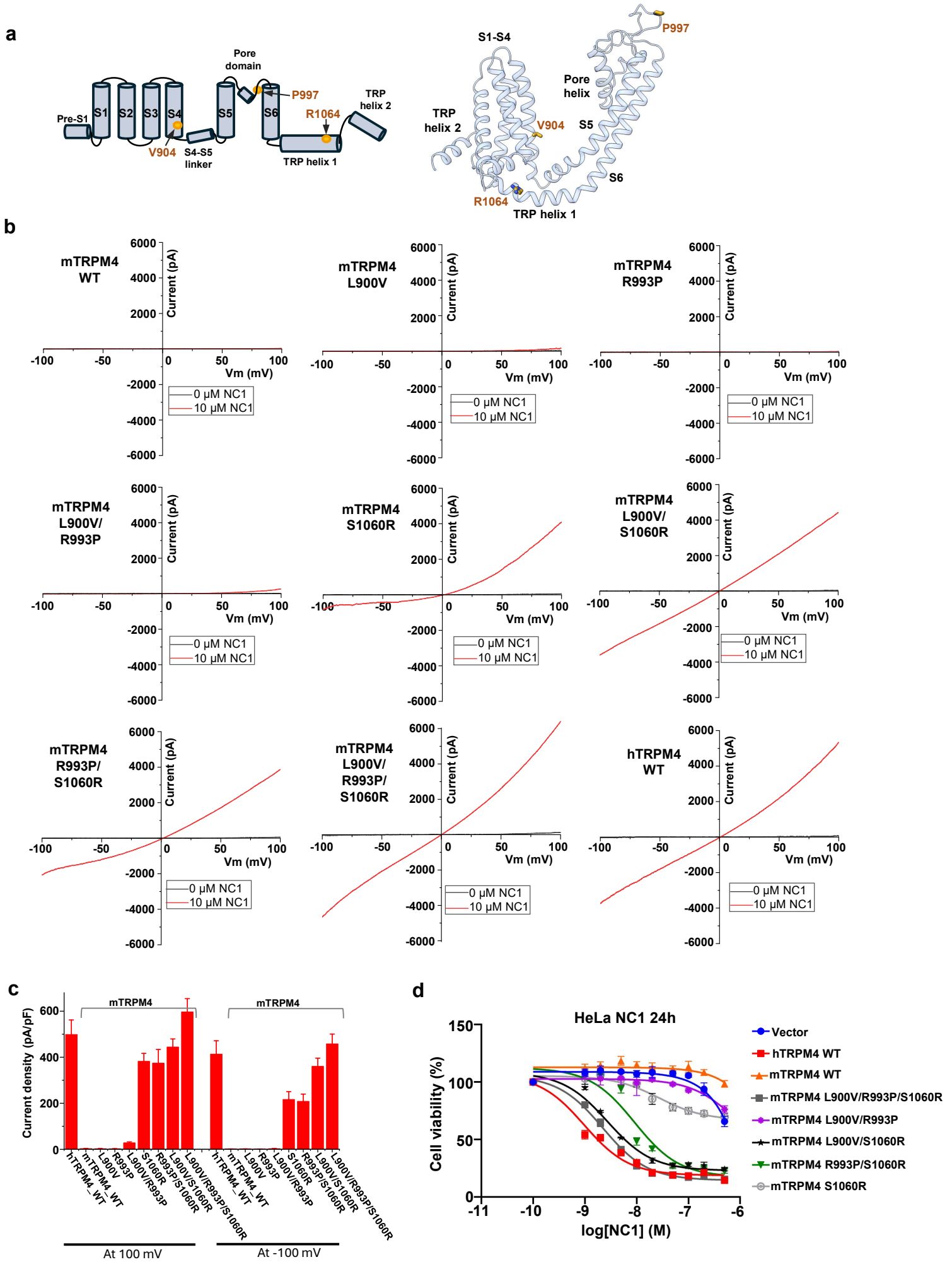
a
Pre-S1
S1
S2
S3
S4
S5
S6
Pore domain
P997
R1064
TRP helix 2
V904
S4-S5 linker
TRP helix 1
S1-S4
Pore helix
S5
S6
b
mTRPM4 WT
mTRPM4 L900V
mTRPM4 R993P
mTRPM4 L900V/ R993P
mTRPM4 S1060R
mTRPM4 L900V/ S1060R
mTRPM4 R993P/ S1060R
mTRPM4 L900V/ R993P/ S1060R
hTRPM4 WT
Current (pA)
Vm (mV)
0 μM NC1
10 μM NC1
c
Current density (pA/pF)
mTRPM4
hTRPM4_WT
mTRPM4_WT
L900V
R993P
L900V/R993P
S1060R
R993P/S1060R
L900V/S1060R
L900V/R993P/S1060R
At 100 mV
At -100 mV
d
HeLa NC1 24h
Cell viability (%)
log[NC1] (M)
Vector
hTRPM4 WT
mTRPM4 WT
mTRPM4 L900V/R993P/S1060R
mTRPM4 L900V/R993P
mTRPM4 L900V/S1060R
mTRPM4 R993P/S1060R
mTRPM4 S1060R

Fig. 6: Molecular determinants of NC1 specificity for human TRPM4. a Topology (left) and structure (right) of the hTRPM4 TM domain with the three key residues important for NC1 specificity marked. **b** Sample I-V curves of wild-type mTRPM4 and its single, double, and triple mutants at the three key residues. Currents were recorded in whole-cell patches with 10 μM NC1 in the bath (extracellular). Current from NC1-activated wild-type hTRPM4 is shown in the last panel for comparison. **c** Outward and inward current densities of the wild-type mTRPM4 and its mutants recorded at ±100 mV in whole-cell patches with 10 μM NC1 in the bath (extracellular). Bars represent mean ± SEM of n=5 independent replicates. Current densities of hTRPM4 are also graphed for comparison. **d** Dose-dependent NC1 cytotoxicity in stable HeLa cell lines expressing wild-type hTRPM4, wild-type mTRPM4, or mTRPM4 mutants. Data points represent mean ± SD of n = 3 independent replicates.

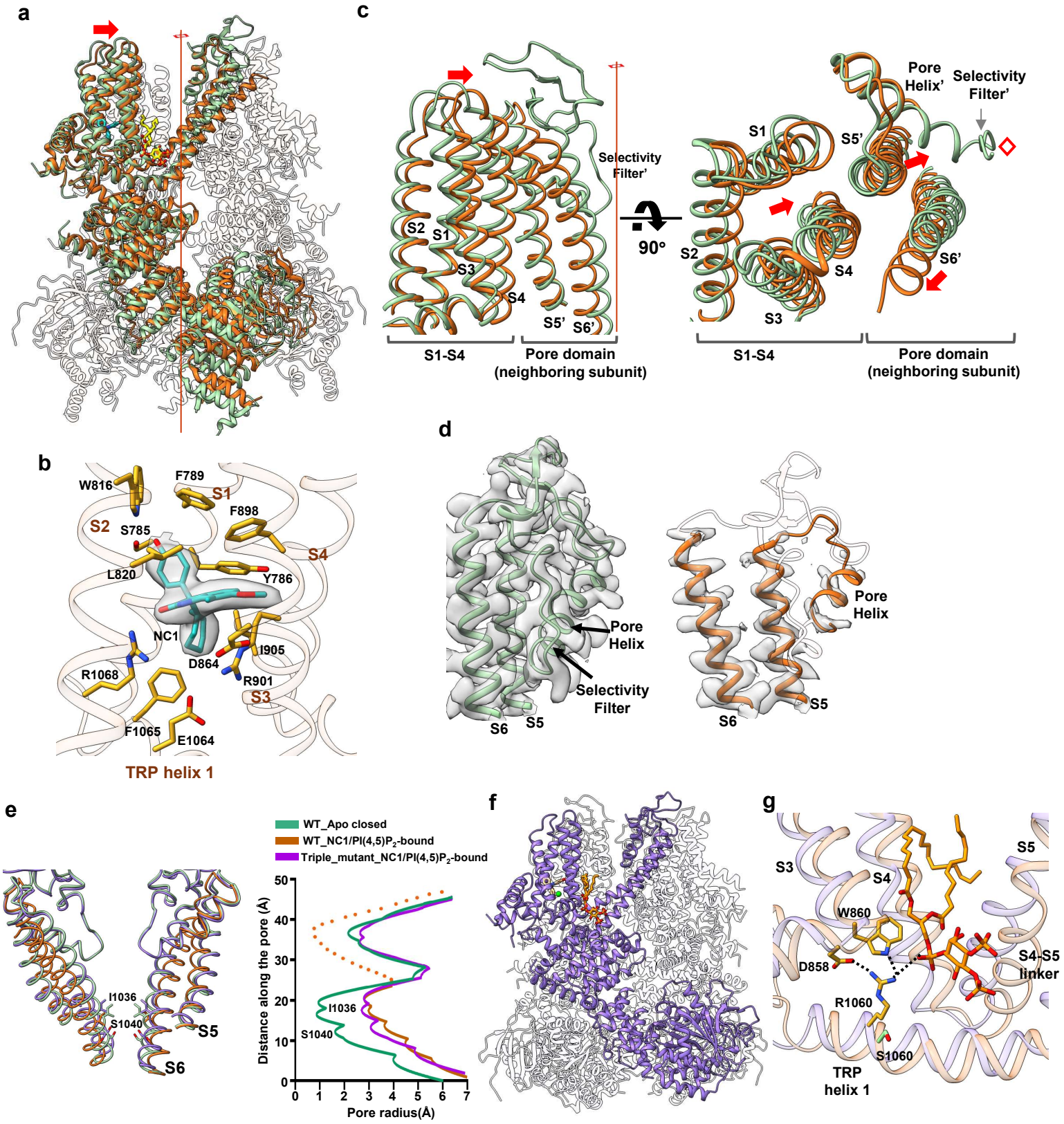
a
c
Selectivity Filter'
S2
S1
S3
S4
S5'
S6'
S1-S4
Pore domain (neighboring subunit)
90°
Pore Helix'
Selectivity Filter'
S1
S5'
S2
S4
S3
S6'
S1-S4
Pore domain (neighboring subunit)
b
W816
F789
S1
F898
S2
S785
S4
L820
Y786
NC1
I905
D864
R1068
R901
S3
F1065
E1064
TRP helix 1
d
Pore Helix
Selectivity Filter
S6
S5
Pore Helix
S5
S6
e
I1036
S1040
S5
S6
WT_Apo closed
WT_NC1/PI(4,5)P2-bound
Triple_mutant_NC1/PI(4,5)P2-bound
Distance along the pore (Å)
Pore radius(Å)
I1036
S1040
f
g
S3
S4
S5
W860
D858
S4-S5 linker
R1060
S1060
TRP helix 1

Fig. 7: NC1 binding in mTRPM4. a Superposition of the NC1/PI(4,5)P_2-bound (brown) and apo closed (PDB:6BCJ) (green) wild-type mTRPM4 structures along the pore axis, with the front subunits highlighted. NC1 (blue) and PI(4,5)P_2 (yellow) are shown in stick representation. **b** Zoomed-in view of the NC1 binding site in mTRPM4. NC1 and its interacting residues are shown in stick representation. NC1 density (grey surface) is contoured at 0.23 in ChimeraX. **c** Conformational changes at S1-S4 and its neighboring pore domain upon NC1 binding to mTRPM4. The red line and red diamond mark the central 4-fold axis. Red arrows indicate the major movements in this region, namely the lateral movement of S1-S4 towards the central axis, the inward movement of the neighboring subunit S5 (S5'), and the outward movement of the neighboring subunit S6 (S6'). **d** Comparison of the density maps at the pore domain between the apo closed (PDB:6bcj) (green) and NC1/PI(4,5)P_2-bound (brown) mTRPM4 structures. The disordered region in the pore domain of the NC1/PI(4,5)P_2-bound structure is depicted as a grey semi-transparent cartoon. **e** Structural comparison of the ion conduction pore in the apo closed (green), NC1/PI(4,5)P_2-bound inactivated (brown) wild-type mTRPM4 and in the NC1/PI(4,5)P_2-bound open (purple) triple mutant (L900V/R993P/S1060R). Gating residues I1036 and S1040 are shown in stick representation. The front and back subunits were removed for clarity. The panel on the right depicts the pore radius along the central axis in these structures. The dotted line illustrates the disordered filter region in the NC1/PI(4,5)P_2-bound wild-type mTRPM4. **f** Structure of the NC1/PI(4,5)P_2-bound mTRPM4 triple mutant (L900V/R993P/S1060R) with the front subunit highlighted in purple. NC1 and PI(4,5)P_2 are shown in stick representation and Ca^{2+} as a green sphere. **g** Structural comparison at S1060 region between NC1/PI(4,5)P_2-bound wild-type mTRPM4 (light brown) and its triple mutant (L900V/R993P/S1060R, light purple). PI(4,5)P_2 and key residues important for stabilizing S1-S4 in the mutant are shown in stick representation. The wild-type S1060 side chain is also shown for comparison.